2011 American Control Conference
on O'Farrell Street, San Francisco, CA, USA
June 29 - July 01, 2011

Lift Force Control of a Flapping-Wing Microrobot

Néstor O. Pérez-Arancibia, John P. Whitney and Robert J. Wood

Abstract— **This paper introduces a methodology for designing real-time controllers capable of enforcing desired trajectories on microrobotic insects in vertical flight and hovering. The main idea considered in this work is that altitude control can be translated into a problem of lift force control. Through analyses and experiments, we describe the proposed control strategy, which is fundamentally adaptive with some elements of model-based control. In order to test and explain the method for controller synthesis and tuning, a static single-wing flapping mechanism is employed in the collection of experimental data. The empirical results validate the suitability of the chosen approach.**

I. Introduction

In [1], the feasibility of flying robotic insects was empirically demonstrated. There, the lift-off of a 60-mg mechanical fly shows that bio-inspired flapping-wing robots can generate lift forces sufficiently large to overcome gravity. However, to date, detailed control strategies addressing experimental altitude control have not been reported. Here, we propose a control scheme and a methodology for synthesizing controllers for the tracking of specified trajectories along the vertical axis. Evidence for the suitability of the considered scheme is provided through experimental results, obtained using the static single-wing flapping mechanism in [2].

The fundamental idea introduced in this work is that enough information about the subsystems composing the robotic insect can be gathered *a priori*, using well-known identification methods, such that, during flight, only an external position sensor is needed. The two main subsystems relevant from a control perspective are the bimorph piezoelectric actuator [3], used to transduce electrical into mechanical power, and the mapping from the actuator's tip displacement to the lift force generated by the passive rotation of the wing, as described in [2].

The dynamics of the system as a whole can be thought of as a dynamic mapping, where the input is the exciting voltage to the actuator and the output is the displacement of the actuator's tip. Note that this representation includes the dynamical interaction of the robot's rigid airframe with all the moving parts in the microrobot, which are the actuator, the transmission mechanism, the wing-hinge and the wing interacting with the air. Clearly, the dynamics of this system are significantly different to the ones exhibit by a physically isolated actuator [4]. Also, note that the displacement-force mapping is an abstract artifact used for design, being physically a complex system composed of the mechanical transmission, the wing-hinge, and the wing interacting with the air to produce lift.

Inspired by nature [5], but also for practical reasons, roboticists have commonly designed flapping-wing mechanisms to be excited by sinusoidal signals, mostly in open-loop configurations (see [1] and references therein). Here, we demonstrate the design and implementation of model-based and model-free controllers, in feedback and feedforward configurations, for following sinusoidal reference signals. The main idea is that, under actuator constrains, frequency, amplitude and phase can be chosen and varied in order to achieve specifications of lift and power. Considering this design choice, a natural control strategy is the implementation of algorithms specialized in dealing with the tracking and rejection of periodic signals. In this category, there are the *internal model principle* (IMP) [6] based algorithms such as those in [7], [8], [9], [10], [11] and other related articles, and also the *adaptive feedforward cancelation* (AFC) algorithms such as those in [12] and [13] and references therein.

As a first approach to the problem, in this work, we adopt a control strategy based on a modified version of the discrete-time ACF algorithm in [12]. Since the AFC algorithm is a disturbance rejection scheme, here, the reference signals to be followed are treated as disturbances to be rejected. As in [12] and [13], the frequencies of the relevant signals are known while the amplitudes and phases are assumed unknown. The idea of treating the amplitudes and phases of sinusoidal references as unknowns seems counterintuitive. However, by the end of the paper, the reason for this approach shall become clear.

The rest of the paper is organized as follows. Section II explains the microrobotic flapping mechanism and the experimental setup. Section III describes the empirical identification of the system dynamics. Section IV discusses the control strategies considered and the controller design method. Section V presents experimental evidence on the suitability of the proposed schemes. Finally, conclusions are given in Section VI.

Notation:

- As usual, $\mathbb{R}$ and $\mathbb{Z}^+$ denote the sets of real and non-negative integer numbers, respectively.
- The variable t is used to index discrete time, i.e., $t = \{kT_s\}_{k=0}^{\infty}$, with $k \in \mathbb{Z}^+$ and $T_s \in \mathbb{R}$. As usual, T_s is referred as the sampling-and-hold time. Depending on the context we might indistinctly write $x(t)$ or $x(k)$.
- z^{-1} denotes the delay operator, i.e., for a signal x, $z^{-1}x(k) = x(k-1)$ and conversely $zx(k) = x(k+1)$. Notice that since some of the systems involved in this paper are time-varying, here, z is not necessarily the complex variable associated to the z-transform.

This work was supported by the Office of Naval Research under Grant N00014-08-1-0919.

The authors are with the School of Engineering and Applied Sciences, Harvard University, Cambridge, MA 02138, USA, and the Wyss Institute for Biologically Inspired Engineering, Harvard University, Boston, MA 02115, USA, (nperez@seas.harvard.edu, jwhitney@fas.harvard.edu, rjwood@eecs.harvard.edu).

II. Motivation and Description of the Experimental System

A. Motivation

An important intermediate objective in our research is the altitude control of a microrobotic fly as the one in [1], depicted in Fig. 1. A fundamental difficulty in achieving this goal is that due to constraints of space and weight, in our first conceptual design, no internal sensors are considered to be mounted in the microrobot. Instead, the design relies on the off-line system identification of two of the subsystems composing the robot, and in some cases, on an external remote position sensor.

It can be shown that the control objective in the previous paragraph can be translated into one of lift force control, and finally as shown in Section IV, reduced to an actuator output control problem. A first thing to notice is that from Fig. 1, the dynamical equation governing the movement of the fly along the vertical axis is simply

$$f_L - mg = m\ddot{x}, \tag{1}$$

where m is the mass of the fly, g is the standard gravity constant and f_L is the instantaneous lift force generated by the flapping of the wings. In some cases, an additional dissipative body drag term $c\dot{x}$ could be added to the right side of (1), where c is a constant to be identified experimentally.

As described in [2], the lift force f_L depends in a nontrivial way, through nonlinear relationships, on the frequency and amplitude of the flapping angle. As also discussed in [2], for sinusoidal inputs, f_L forces typically oscillate around some non-zero mean force crossing zero periodically. Therefore, positive vertical motion occurs when in average the lift force f_L is larger that mg. When using digital computers, for acquisition and control, f_L will be sampled at a fixed sampling rate. Therefore, mathematically, the average force can be approximated as

$$F_L^{(N_L)}(t) = F_L^{(N_L)}(kT_s) = F_L^{(N_L)}(k) = \frac{1}{N_L}\sum_{i=0}^{N_L-1} f_L(k-i), \tag{2}$$

where, $0 < N_L \in \mathbb{Z}^+$. Often, the superscript (N_L) will be dropped and we will simply write $F_L(t)$, if N_L is obvious from the context.

Thus, the key element in our control strategy is the capability of forcing the average lift force signal in (2) to follow a specified reference. In order to develop a general methodology to be applied to any flapping-wing microrobot of the kind depicted in Fig. 1, here, we propose and study algorithms and techniques for identifying the plants of the relevant subsystems and for tuning the necessary parameters involved. This is done empirically, using a modified version of the experimental setup in [2], which is discussed in the next subsection.

B. Experimental Setup

We use the experimental setup in Fig. 2, which is a modified version of the one in [2]. This setup was constructed for the simultaneous measurement of lift forces generated by a flapping mechanism and identification of the resulting system dynamics from the perspective of the mounted bimorph actuator, employed to drive the microrobotic system. In Fig. 2, it can be observed that the wing driver mechanism is mounted on the end of a double-cantilever beam, whose deflection is measured with a *capacitive displacement sensor* (CDS). From solid mechanics principles, for small beam deflections, there exists a linear relationship between deflection and lift force.

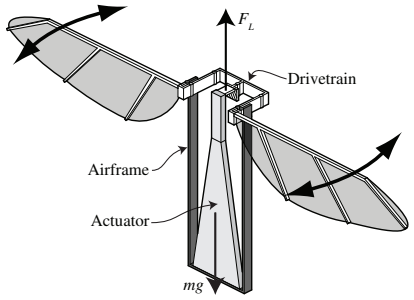

Fig. 1. Illustration of typical Harvard microrobotic fly, similar to the one in [1]. This particular design is described in [14] (drawing courtesy of P. S. Sreetharan).

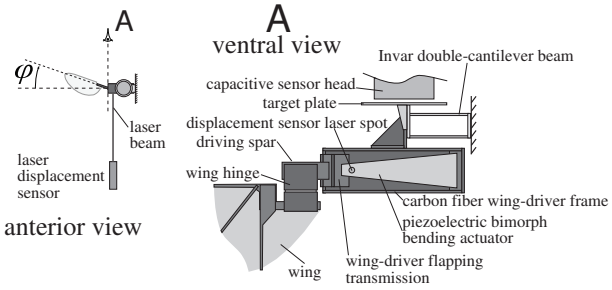

Fig. 2. Diagram of experimental setup used for measuring instantaneous lift forces and displacements of the actuator's tip. The wing-driver is attached to an Invar double-cantilever beam, whose deflection is measured by a capacitive displacement sensor. This deflection is proportional to the lift force, for small deformations of the beam. The displacement of the actuator's tip is measured using a CCD laser displacement sensor. For details on the force sensor see [15].

The piezoelectric bimorph actuator, mounted in a carbon fiber frame, used for flapping the wing is similar to the one described in [3]. The linear displacement of the drive actuator's tip is mapped to an angular flapping motion employing a transmission mechanism of the type described in [1]. The resulting flapping angle is labeled by φ in Fig. 2. Notice that as explained in [2], flapping induces the flexure of the wing-hinge, generating the passive rotation that in turn produces lift. In order to minimize the effective mass of the beam-driver system, the actuator is fabricated as light as possible, thus maximizing the sensor bandwidth. Further details on the design, fabrication and calibration of the CDS-based force sensor are given in [2] and [15].

The other variable measured is the displacement of the actuator's tip. As shown in Fig. 2, this is done using a non-contact CCD[1] laser displacement sensor, which is located to a close distance from the actuator's tip. In order

[1] *Charge-coupled device.*

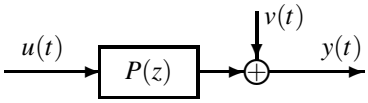

Fig. 3. Idealized system dynamics. $P(z)$: Identified discrete-time open-loop plant; $u(t)$: Input voltage signal to the actuator; $y(t)$: Output displacement of the actuator's tip; $v(t)$: Output disturbance, representing the aggregated effects of all the disturbances affecting the system, including the unmodeled nonlinear aerodynamic forces produced by the wing flapping.

to determine the measurement, the sensor uses an optical triangulation principle. Specifically, a semiconductor laser beam is reflected off the target surface and passes through a receiver lens system. Then, the beam is focused on a CCD sensing array, which detects the peak value of the light distribution of the beam spot. The CCD pixels within the area of the beam spot are used to determine target position. As the target displacement changes relative to the sensor head, the reflected beam position changes on the CCD array. In Fig. 2, the sensor laser reflection on the actuator is depicted as a circular spot.

III. System Identification for Controller Design

A. Identification of the System Dynamics

The flapping mechanism described in Section II can be seen, from the piezoelectric actuator perspective, as a system in which the input is the voltage signal feeding the actuator and the output is the displacement of the actuator's tip measured using the CCD laser displacement sensor. In this approach the output disturbance $v(t)$ represents the aggregated effects of all the disturbances affecting the system, including the unmodeled nonlinear aerodynamic forces produced by the wing flapping. With this idea in mind, as depicted in Fig. 3, a discrete-time representation of the system can be found using *linear time-invariant* (LTI) system identification methods. Note that the dynamics of this system are significantly different to the ones exhibit by a physically isolated actuator [4]

Here, using the algorithm in [16], according to the implementation described in [17] and [18], the system in Fig. 3 is identified, with the use of $200,000$ samples generated using a white-noise signal input $u(t)$, at a sampling-and-hold rate of 10 KHz. It is important to mention that due to variability in the micro-fabrication process, the models shown in this article are used to illustrate the proposed identification and control strategies, but they do not necessarily represent the typical dynamics of flapping systems.

The identified dynamics of $P(z)$, labeled as $\hat{P}(z)$, are shown in Fig. 4. There, the original 48th-order model is shown along with reduced models with orders 12 and 4, respectively. Notice that the identified systems have been normalized so that the respective DC gain is 0 dB. The natural frequency of $\hat{P}(z)$ is 118.36 Hz. As usual, in order to reduce the system, a state-space realization of the identified 48th-order model is balanced [19], and then, a certain number of states, relatively less observable and controllable than the others, are discarded. For theoretical details see [19] and [20]; for comments on an experimental implementation see [17] and [18].

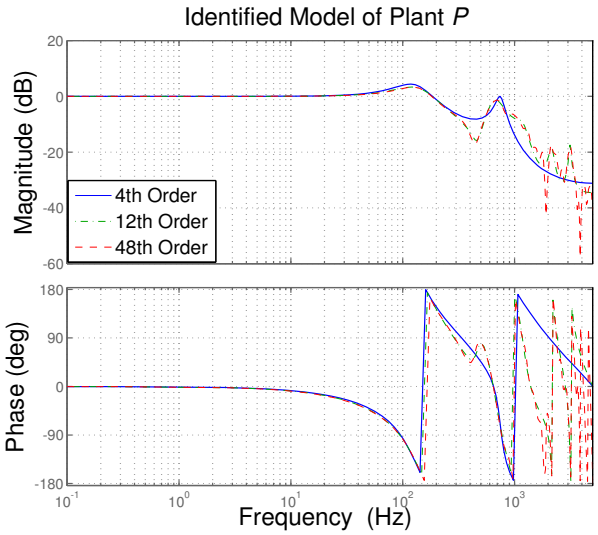

Fig. 4. Bode diagram of identified model $\hat{P}(z)$ of the plant $P(z)$. A 48th-order model is shown in red, reduced 12th and 4th order models are shown in green and blue, respectively.

IV. Control Strategies

A. Displacement Control of the Actuator's Tip

As explained in Section II, in order for a robotic insect to accurately follow a desired trajectory, a reference of the average lift force, $F_L(t)$, must be followed. In the next subsection, we show that an empirical relationship between average lift force and amplitude of the actuator tip displacement, for a fixed frequency, can be found. A way of thinking of this relationship is as a lookup table, with which, for a given frequency, a desired average lift force is mapped into a desired amplitude to be followed by the actuator's tip.

In order to implement a feedback control loop around $P(z)$, a measurement of the actuator's tip displacement is required. However, in that case, a plant model is not strictly necessary for implementing the controller in real-time. On the other hand, employing the identified plant $\hat{P}(z)$ in Fig. 4, a model-based feedforward strategy can be pursued. A feedback control strategy is convenient in cases in which precision and accuracy are required. For example, when performing experiments in which relationships between actuator displacement and average lift force are estimated. A model-based feedforward strategy will be essential for the implementation of real-time controllers on systems in which the use of displacement sensors is infeasible with the available technology. For example, it is unrealistic to think that a reliable displacement sensor could be mounted in a flying microrobotic insect.

For reasons already commented, in both feedback and model-based feedforward configurations, the desired outputs from the system $P(z)$ have the form

$$y_d(k) = a(k)\sin\left(\frac{2\pi k}{N}\right) + b(k)\cos\left(\frac{2\pi k}{N}\right), \qquad (3)$$

where N is the number of samples per cycle, and $a(k)$ and $b(k)$ are considered to be unknown functions of time. The

frequency is considered known. It is somehow counterintuitive to think of a reference as a partially unknown signal. However, this approach is convenient because in the lift force control experiments, the actuator displacement reference is generated in real-time according to a lookup table to be discussed in the next subsection, and therefore, unknown *a priori*. As discussed in the Introduction, here we use a slightly modified version of the discrete-time AFC algorithm in [12], which is an Euler method-based approximation of the continuous-time AFC algorithm studied in [21]. The proposed control scheme is shown in Fig. 5. For purposes of analysis, let us for now assume that $v(k) = 0,\ \forall\ k$. Then, the main idea behind the algorithm is that if the signal

$$r(k) = -y_d(k) \tag{4}$$

is rejected effectively, it follows that the error

$$e(k) = y(k) + r(k) = [Pu](k) + r(k) \tag{5}$$

is minimized. Consequently, if the error $e(k)$ in (5) is minimized, the system output $y(k)$ closely follows the reference $y_d(k)$.

Ideally, for a stable minimum phase plant P, in order to cancel $r(k)$, the control signal should be $u(k) = -\left[P^{-1}\hat{r}\right](k)$, where $\hat{r}(k)$ is an estimate of $r(k)$. However, most systems are non-minimum phase, in which instances, the best minimum phase approximation of $P(z)$, $\bar{P}(z)$, should be used. In that case, $\bar{P}^{-1}$ would produce an unwanted effect on the magnitude and phase of $\hat{r}(k)$. Fortunately, since the magnitude and phase of the periodic signal $r(k)$ are being estimated adaptively, the system inverse can be ignored and the new control signal simply becomes

$$u(k) = -\left[\hat{\alpha}(k)\sin\left(\frac{2\pi k}{N}\right) + \hat{\beta}(k)\cos\left(\frac{2\pi k}{N}\right)\right], \tag{6}$$

with the adaptive law

$$\hat{\alpha}(k) = \hat{\alpha}(k-1) + \gamma e(k-1)\sin\left(\frac{2\pi k}{N} + \phi\right), \tag{7}$$

$$\hat{\beta}(k) = \hat{\beta}(k-1) + \gamma e(k-1)\cos\left(\frac{2\pi k}{N} + \phi\right), \tag{8}$$

where $y(k)$ is the measured actuator's tip displacement, and according to (5), $e(k-1) = y(k-1) + r(k-1)$. The symbol γ represents an adaptation gain, chosen by simulation, using a computer model of the system depicted in Fig. 5. The phase parameter ϕ is also chosen by simulation.

In this article, we introduce the notion that the reference signal $r(k)$ in Fig. 5 can be seen as an output disturbance, and therefore, that the reference-following problem considered here is very similar to the disturbance rejection case in [13]. Note that since $u(k)$ is filtered through $P(z)$, $\hat{\alpha}(k)$ and $\hat{\beta}(k)$ are not estimates of $a(k)$ and $b(k)$, respectively. Nonetheless, as explained in [13], the ideas on stability and convergence, for the input disturbance case, discussed in [12] and references therein, apply to this case.

Later in this section, we will show that a significant part of the frequency content of the disturbances affecting the microrobotic flapping-wing system, for a sinusoidal $r(k)$, modeled as the output disturbance $v(t)$, is the result of

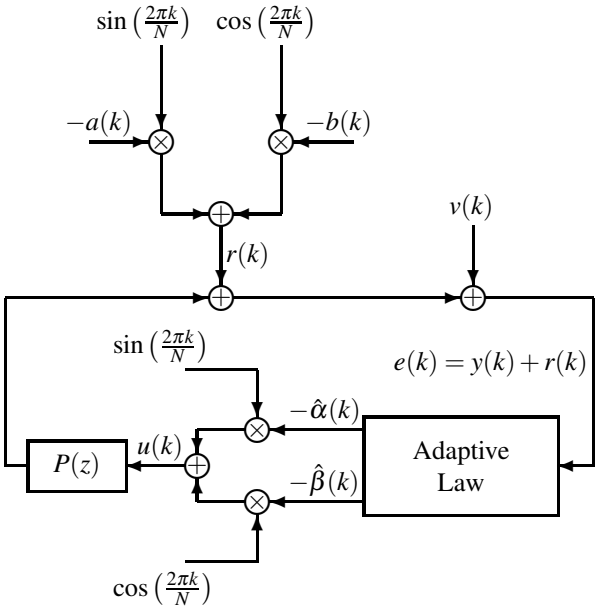

Fig. 5. AFC scheme for rejecting $r(k)$ and tracking $y_d(t)$.

harmonics of the fundamental frequency f_r, where f_r is the frequency of the periodic signal $r(t) = r(kT_s) = r(k)$ in Fig. 5. This nonlinear effect can be modeled by connecting a linear model and a polynomial mapping in a so-called Volterra configuration. However, a compelling physical explanation behind this phenomenon is still lacking and these issues remain a matter of further research. Nonetheless, it is important to mention that the appearance of harmonics in natural insects has been reported [5], which suggests that there might be a fluid mechanics explanation of the phenomenon.

Disturbance profiles of this kind are reminiscent of the repeatable runout described in the *hard disk drive* (HDD) literature (see [12], [13], [11] and references therein). Thus, it is possible that the reasons for the appearance of harmonic disturbances in this case are similar to ones in the HDD case. Though the causes of this phenomenon are relevant to the physics of the particular system, they are not necessary for the implementation of a scheme capable of rejecting them. Thus, let us assume that

$$\begin{aligned} d(k) &= r(k) + v(k) \\ &= \sum_{i=1}^{n}\left[a_i(k)\sin\left(\frac{2\pi ik}{N}\right) + b_i(k)\cos\left(\frac{2\pi ik}{N}\right)\right], \end{aligned} \tag{9}$$

where i is the index for the corresponding harmonic, N is the number of samples per cycle, and the reference signal is relabeled as $r(k) = a_1(k)\sin\left(\frac{2\pi k}{N}\right) + b_1(k)\cos\left(\frac{2\pi k}{N}\right)$. Obviously, the other components of $d(k)$ in (9) are assumed to be part of $v(k)$.

Everything argued in the previous paragraphs, for the case $d(k) = r(k)$, is fundamentally valid for the case in which $d(k) = r(k) + v(k)$ with the form in (9). Thus, as in [13], a canceling control signal for the case in (9) is

$$u(k) = -\sum_{i=1}^{n}\left[\hat{\alpha}_i(k)\sin\left(\frac{2\pi ik}{N}\right) + \hat{\beta}_i(k)\cos\left(\frac{2\pi ik}{N}\right)\right]. \tag{10}$$

The update equations for the estimated parameters become

$$\hat{\alpha}_i(k) = \hat{\alpha}_i(k-1) + \gamma_i e(k-1)\sin\left(\frac{2\pi ik}{N} + \phi_i\right), \qquad (11)$$

$$\hat{\beta}_i(k) = \hat{\beta}_i(k-1) + \gamma_i e(k-1)\cos\left(\frac{2\pi ik}{N} + \phi_i\right), \qquad (12)$$

where the γ_i are adaptation gains, chosen differently for each harmonic. A phase advance modification can be added to reduce the sensitivity and allow for more harmonics to be canceled as was done previously in [12] and [13], if necessary. Sometimes it is convenient to choose $\phi_i = \angle P(e^{j\theta_i})$, with $\theta_i = 2\pi i\left(\frac{f_r}{f_s}\right)$, where f_r and f_s are the frequency of $r(t)$ and the sampling frequency of the system, respectively. As in the case where $d(k) = r(k)$, in this case, $\hat{\alpha}_i(k)$ and $\hat{\beta}_i(k)$ are not estimates of $a_i(k)$ and $b_i(k)$, respectively.

Following the method in [12], and as done in [13], the adaptive feedforward disturbance rejection scheme in Fig. 5 can be transformed into an LTI equivalent representation. By treating the rejection scheme as an LTI system, the sensitivity function from $d(k)$ to $e(k)$ can be computed, allowing a performance evaluation of the whole system. Here, this analysis is omitted because it can be easily done following the example in [13].

Due to limitations of space and weight, it is currently unreasonable to design a flying microrobot under the assumption that internal sensors can be mounted into the device. Therefore, here we explore the feasibility of implementing the scheme considered in Fig. 5 after replacing sensors by identified models, as shown in Fig. 6. There, the control signal $u(k)$ is used as input to the system plant, $P(z)$, and also to an identified model of it, $\hat{P}(z)$. Instead of using the measured signal $y(k)$ to update the gains $\hat{\alpha}(k)$ and $\hat{\beta}(k)$, an estimate of $y(k)$, $\hat{y}(k)$, is used for that purpose.

In order to demonstrate the suitability of the proposed methods, here we show four experimental cases, in Figs. 7, 8, 9 and 10, respectively. The first case is shown for purposes of analysis and comparison, in which no control is applied to the system. Here, the system is excited in open loop by a sinusoidal signal $u(t) = y_d(t) = A_r\sin(2\pi f_r t)$ with normalized amplitude $A_r = 1$ and frequency $f_r = 105$ Hz. The normalization is such that a constant input $u(t) = 1$ generates an output equal to 1.

Three things should be noticed in Fig. 7. The first is that the system can be approximated by the use of a linear model. This is clear from the fact that the *power spectral density* (PSD) estimate of the output $y(t)$ shows that most of the signal power is concentrated at the fundamental frequency of the reference, 105 Hz. The second is that, as expected, the phase and magnitude of the output are changed with respect to the input. The third is that a pattern of harmonics appears in the output signal's PSD. As explained before, the physics of the underlying phenomenon is not completely understood. However, these harmonics can be treated as output disturbances affecting the system.

Cases 2 and 3 are shown in Figs. 8 and 9, respectively. In these cases, $y_d(t) = A_r\sin(2\pi f_r t)$ and $r(t) = -y_d(t)$, with $A_r = 1$ and $f_r = 105$ Hz. Case 2 is the implementation of the adaptive scheme in Fig. 5, with the adaptive law in (6), (7) and (8). Clearly, the control strategy is capable of correcting for the phase shift and magnitude amplification, but as expected, the harmonics remain essentially the same of Case 1. Case 3 is the implementation of the adaptive scheme with the adaptive law in (10), (11) and (12), which from this point onwards is referred as *harmonic rejection scheme* (HRS). Unequivocally, the control method is capable of correcting for the phase shift, the magnitude amplification, and also to reject the first three harmonics, targeted in this experiment. This is evidenced by the bottom plot of Fig. 9, which compares the PSD estimates of the measured outputs $y(t)$, with and without using the HRS.

Finally, Case 4 is shown in Fig. 10. This is the implementation of the model-based AFC scheme in Fig. 6, with the same desired output $y_d(t)$ of Case 2. Due to discrepancies between the model $\hat{P}(z)$ and the physical system $P(z)$, the performance is degraded respect to the ones obtained using the scheme in Fig. 5 and the HRS. However, this degradation is not significant in the context of this research. The control errors are summarized in Table I.

TABLE I
RMS VALUE OF THE CONTROL ERROR SIGNAL $e(k)$, FOR FOUR EXPERIMENTAL CASES

Case	1	2	3	4
RMS value	1.2107	0.1417	0.0867	0.1735

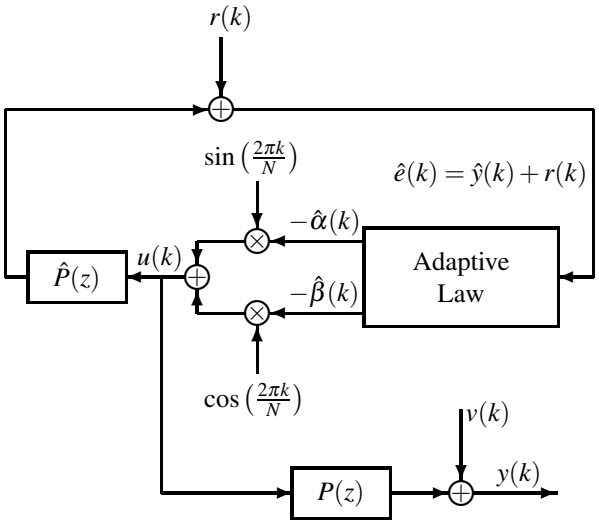

Fig. 6. Model-based AFC scheme for rejecting $r(k)$ and tracking $y_d(t)$.

B. Empirical Relationship Between the Actuator Tip's Displacement and Lift Force

The considered control strategy relies on rejecting the signal $r(k)$ by the use of the fully adaptive scheme in Fig. 5 or the model-based adaptive scheme in Fig. 6. In order to generate a signal $r(t) = -y_d(t) = -A_r\sin(2\pi f_r t)$ with the appropriate phase and amplitude required for generating a desired average lift force profile, in this subsection we present an experimental method for finding a lookup table

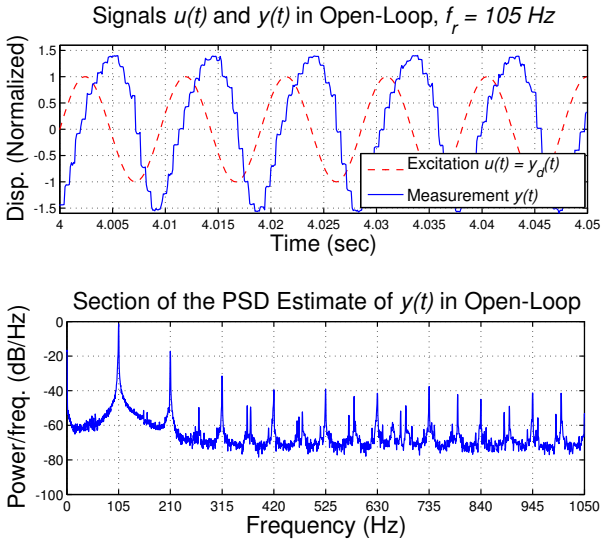

Fig. 7. **Case 1.** *Upper Plot:* Time series of $u(t) = A_r \sin(2\pi f_r t)$ and $y(t)$ in open loop, with $A_r = 1$ and $f_r = 105$ Hz. *Bottom Plot:* PSD estimate of the measured output $y(t)$ in open loop.

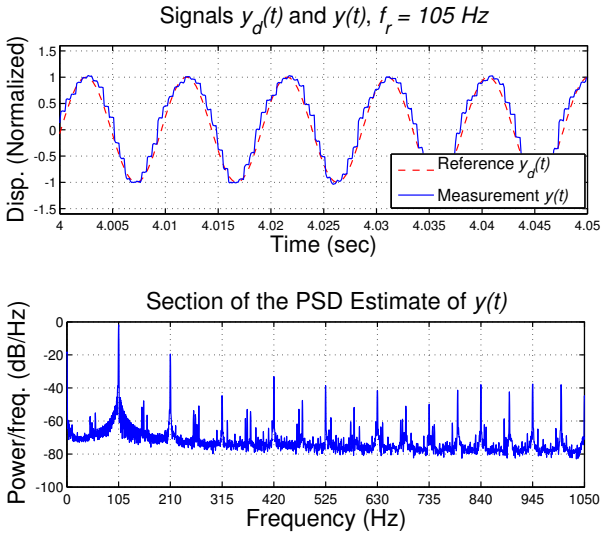

Fig. 8. **Case 2.** *Upper Plot:* Time series of $y_d(t) = A_r \sin(2\pi f_r t)$ and $y(t)$, using adaptive scheme in Fig. 5, with $A_r = 1$ and $f_r = 105$ Hz. *Bottom Plot:* PSD estimate of the measured output $y(t)$.

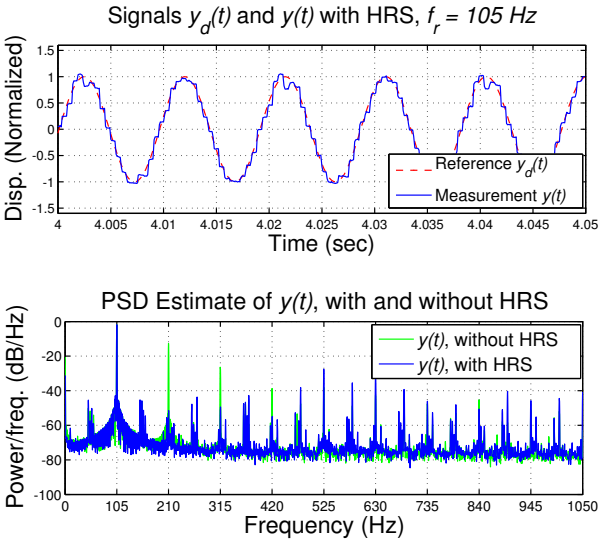

Fig. 9. **Case 3.** *Upper Plot:* Time series of $y_d(t) = A_r \sin(2\pi f_r t)$ and $y(t)$, using the HRS, with $A_r = 1$ and $f_r = 105$ Hz. *Bottom Plot:* Comparison of the estimated PSDs of the measured outputs $y(t)$, with and without using the HRS.

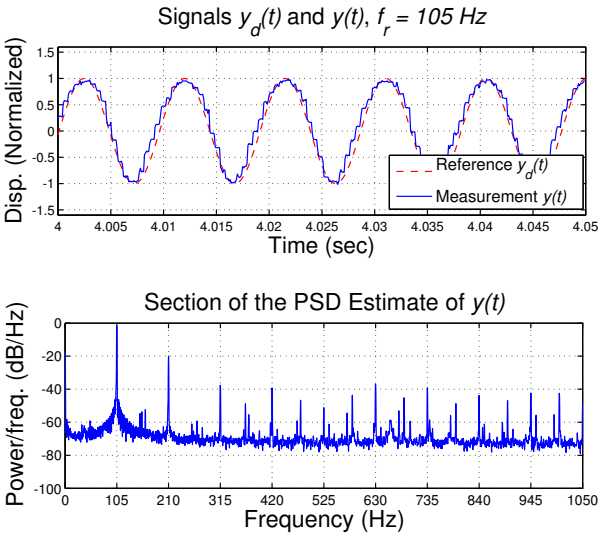

Fig. 10. **Case 4.** *Upper Plot:* Time series of $y_d(t) = A_r \sin(2\pi f_r t)$ and $y(t)$, using the model-based adaptive scheme in Fig. 6, with $A_r = 1$ and $f_r = 105$ Hz. *Bottom Plot:* PSD estimate of the measured output $y(t)$.

that maps the amplitude of the output signal $y(t)$ to the average lift force $F_L(t)$, for fixed frequencies.

Arbitrarily, we pick five fixed values for the frequency f_r, 105, 120, 135, 150 and 180 Hz, and within these drive frequencies, the amplitude of $r(t)$ is varied. Using the fully adaptive scheme in Fig. 5, we ensure that the actual output $y(t)$ rejects and follows the chosen $r(t)$ and $y_d(t)$, respectively. Then, using the force sensor described in Section II, for a fixed frequency and a given amplitude, the average lift force is measured. For example, Fig. 11 shows the instantaneous and average forces when $f_r = 105$ Hz, the amplitude of $y_d(t)$ is equal to 1.2 and $N_L = 1{,}000$. Repeating the experiment for different amplitudes, a mapping describing the amplitude-force relationship can be found. Thus, for $f_r = 105$ Hz, in Fig. 12 each symbol $\star$ represents an experiment in which 200,000 data points were collected. Here, it can be observed that the average lift force varies roughly in a linear manner on the amplitude of the signal $r(t)$. Then, using the least-squares method, a line is fitted to the data. This is shown as a dashed red line.

Besides its rough linearity, another remarkable feature of the relationship between average lift force and the amplitude of $r(t)$ is that the rightmost data-point $\star$ marks the maximum actuator displacement amplitude achievable at the frequency $f_r = 105$ Hz. The hard physical constraint is the amplitude of the control signal $u(t)$ that feeds the amplifier connecting the digital controller to the bimorph piezoelectric actuator.

TABLE II

RMS VALUE OF CONTROL SIGNAL $u(k)$, REQUIRED FOR GENERATING 35 *mg* OF LIFT FORCE

f_r	105 Hz	120 Hz	135 Hz	150 Hz	180 Hz
RMS value	Infeasible	0.9340	0.8606	0.7521	0.9408

This signal cannot exceed 1 V, because it is amplified by a factor of 100 and biased by 100 V before being fed to the actuator, which by design does not tolerate voltages larger than 200 V. Thus, the maximum feasible amplitude of $y_d(t)$ depends on the frequency f_r, and can be easily estimated by looking at the Bode plot of the identified plant $\hat{P}(z)$ in Fig. 3. For further details on the actuator's physics see [3].

The same experiment was repeated with f_r taking the values 120, 135, 150 and 180 Hz. The corresponding data points and fitted lines are shown in Fig. 12. Around the natural frequency of the system $P(z)$, increasing the frequency f_r, increases the magnitude of the average lift force. This is consistent with the idea that for certain frequency ranges, the passive rotation of the wing around the wing hinge is increased, producing stronger lift forces. As discussed in [2], and mentioned earlier in this article, the dynamics describing the relationship between flapping signals and lift forces are highly nonlinear. Therefore, the data shown here are for illustrating the proposed control scheme, and not for explaining a physical phenomenon, since these results are contingent to this particular experimental case.

With the previous comments in mind, a second thing to notice is that it is not necessarily the best control strategy to choose f_r equal to the natural frequency of $P(z)$. For example, among the options in Fig. 12, the best choice is $f_r = 150$ Hz. To explain this, consider the hypothetical case of a 70-mg fly, in which each wing should produce more than 35 mg of average lift force to cause a vertical ascent of the microrobot. Clearly, more than 35 mg can be generated with amplitude 1 and $f_r = 180$ Hz, amplitude 1.1 and $f_r = 150$ Hz, amplitude 1.4 and $f_r = 135$ Hz, and amplitude 1.6 and $f_r = 120$ Hz. Notice that it is infeasible to generate a force larger than 35 mg with $f_r = 105$ Hz. Therefore, the obvious choice is $f_r = 150$ Hz, because it is not only possible to generate an average lift force larger than 35 mg, but also because the maximum achievable force exceeds 50 mg, allowing a greater maneuverability. The RMS values of the required control signals for producing 35 mg are summarized in Table II. Notice that the required signal with smallest RMS value corresponds to the case $f_r = 150$ Hz.

The purpose of finding an empirical relationship between the actuator tip displacement and the generated average lift force is schematized in Fig. 13. Here, $x(t)$ is the altitude of a fly as modeled in Subsection II.A, measured using an external sensor or camera and $x_d(t)$ is the desired vertical trajectory. Using $x_d(t)$ or $e_x(t) = x_d(t) - x(t)$ and an upper level control law, a desired average lift force $F_L(t)$ can be generated. Then, using a lookup table, obtained empirically as was done in Fig. 12, $F_L(t)$ is mapped to a desired reference

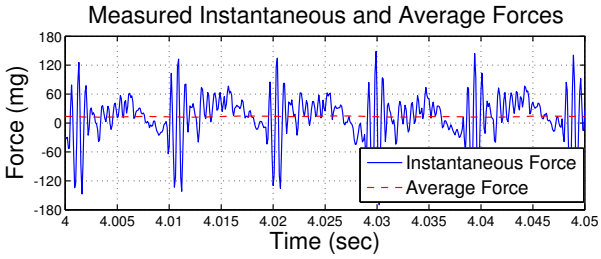

Fig. 11. Example showing instantaneous and average forces.

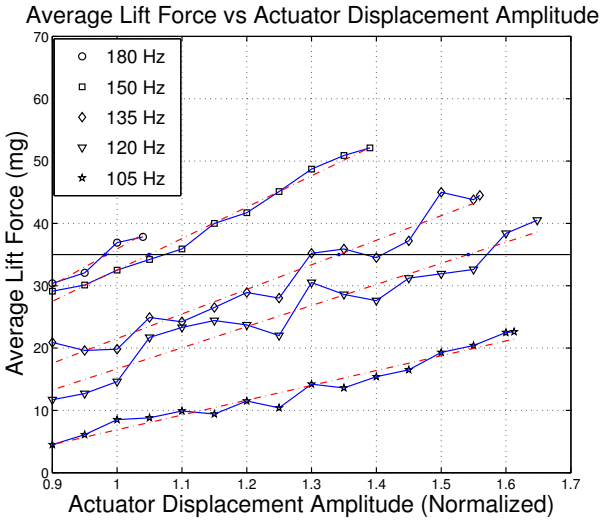

Fig. 12. Empirical relationship between the average lift force and the actuator's tip displacement amplitude, with f_r taking the values 105, 120, 135, 150 and 180 Hz.

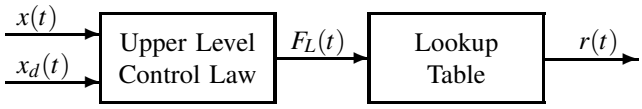

Fig. 13. Depiction of an upper level altitude control strategy.

$r(t)$ to be used in the scheme in Fig. 6. An experimental example is described in the next section.

V. EXPERIMENTAL LIFT FORCE CONTROL EXAMPLE

In this section, we present an experimental example of altitude control. Since the main idea is to demonstrate lift control using the adaptive scheme in Fig. 6, we employ a simple open-loop upper level control law. The objective is to follow an average lift force signal, $F_L(t)$, such that a 70-mg robotic fly would move from 0 to 0.3 m and then return to 0 m in no more than 3 s. Using the model in Subsection II.A and the experimental data obtained for plotting Fig. 12, through computer simulation the complying *a priori* trajectory in Fig. 14 was found. Also according to the simulation, the *a priori* trajectory in Fig. 14 is achievable by tracking the desired average lift force signal in red in Fig. 15, where $N_L = 1,000$.

The resulting experimental average lift force is plotted in blue in Fig. 15, which using the control strategy in Section IV, results from choosing $r(t) = -y_d(t) =$

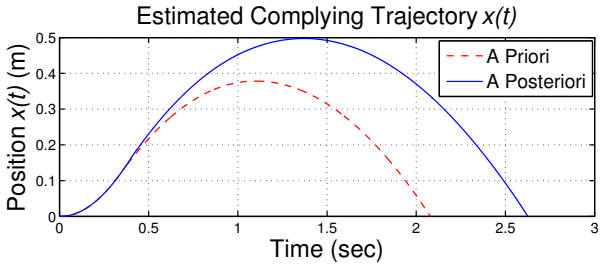

Fig. 14. *A priori* and *a posteriori* estimated corresponding trajectories.

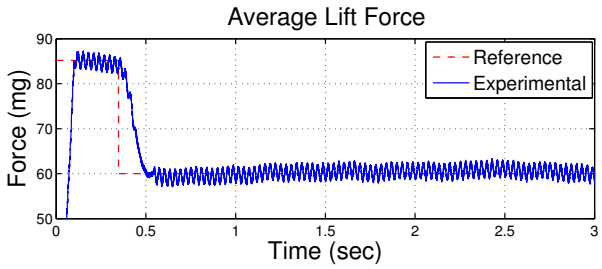

Fig. 15. Reference and experimentally obtained average lift force.

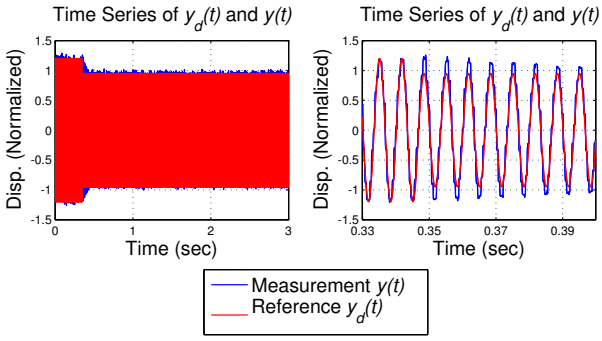

Fig. 16. Comparison of the time series of the experimental $y_d(t)$ and $y(t)$ generating the average lift force in Fig. 15. *Left Plot:* Complete series. *Right Plot:* Transition from $A_r = 1.2$ to $A_r = 0.95$.

$-A_r \sin(2\pi 150t)$, with $A_r = 1.2$ for $t \in [0, 0.347)$ s and $A_r = 0.95$ for $t \in [0.347, 5]$ s. The time series of the experimental reference, $y_d(t)$, and output, $y(t)$, are shown in Fig. 16. Here, on the left the complete signals are compared, and on the right the transition from $A_r = 1.2$ to $A_r = 0.95$ is shown. Notice that $y(t)$ is capable of following $y_d(t)$ and that the transition is smooth, because $P(z)$ is under the control of the feedforward scheme in Fig. 6. According to the simulations, the estimated resulting *a posteriori* trajectory is shown in blue in Fig. 14, which indicates that more elaborated upper level control laws are required for achieving complex trajectories.

VI. Conclusion and Future Work

In this paper, we presented an investigation on the issue of enforcing desired trajectories on microrobotic insects in vertical flight and hovering. We argued, using analyses and experimental data, that the original problem can be converted into one of average force lift control, and finally, into one of displacement tracking of the bimorph actuator's tip. In order to test the concepts introduced here, we used a single-wing static flapping mechanism. In the future, we will further investigate several issues that remain open, among others, the design of upper-level control strategies, the nonlinear modeling of the mapping from actuator's tip displacement to lift force, and the experimental implementation of the control strategy into a two-wing fly in vertical motion and hovering.

References

[1] R. J. Wood, "The First Takeoff of a Biologically Inspired At-Scale Robotic Insect," *IEEE Trans. Robot.*, vol. 24, no. 2, pp. 341–347, Apr. 2008.

[2] J. P. Whitney and R. J. Wood, "Aeromechanics of passive rotation in flapping flight," *J. Fluid Mech.*, vol. 660, pp. 197–220, Oct. 2010.

[3] R. J. Wood, E. Steltz, and R. S. Fearing, "Nonlinear Performance Limits for High Energy Density Piezoelectric Bending Actuators," in *Proc. IEEE Int. Conf. Robot. Autom.*, Barcelona, Spain, Apr. 2005, pp. 3633–3640.

[4] B. M. Finio, N. O. Pérez-Arancibia, and R. J. Wood, "System identification, modeling, and optimization of an insect-sized flapping-wing micro air vehicle," submitted to *IEEE/RSJ Int. Conf. Intell. Robots Syst.*, San Francisco, CA, Sep. 2011.

[5] R. Dudley, *The Biomechanics of Insect Flight*. Princeton, NJ: Princeton University Press, 2000.

[6] B. A. Francis and W. M. Wonham, "The internal model principle of control theory," *Automatica*, vol. 12, no. 5, pp. 457–465, Sep. 1976.

[7] M. Tomizuka, T.-C. Tsao, and K.-K. Chew, "Analysis and Synthesis of Discrete-Time Repetitive Controllers," *ASME J. Dyn. Syst., Meas., Control*, vol. 111, no. 3, pp. 353–358, Sep. 1989.

[8] M. Tomizuka, "Zero Phase Error Tracking Algorithm for Digital Control," *ASME J. Dyn. Syst., Meas., Control*, vol. 111, no. 1, pp. 65–68, Mar. 1987.

[9] S. Hara, Y. Yamamoto, T. Omata, and M. Nakano, "Repetitive Control System: A New Type Servo System for Periodic Exogenous Signals," *IEEE Trans. Autom. Control*, vol. 33, no. 7, pp. 659–668, Jul. 1998.

[10] T. Inoue, M. Nakano, T. Kubo, S. Matsumoto, and H. Baba, "High Accuracy Control of a Proton Synchrotron Magnet Power Supply," in *Proc. IFAC World Congress*, Kyoto, Japan, Aug. 1981, pp. 3137–3142.

[11] N. O. Pérez-Arancibia, T.-C. Tsao, and J. S. Gibson, "A new method for synthesizing multiple-period adaptive–repetitive controllers and its application to the control of hard disk drives," *Automatica*, vol. 46, no. 7, pp. 1186–1195, Jul. 2010.

[12] A. Sacks, M. Bodson, and P. Khosla, "Experimental Results of Adaptive Periodic Disturbance Cancellation in a High Performance Magnetic Disk Drive," *ASME J. Dyn. Syst., Meas., Control*, vol. 118, no. 3, pp. 416–424, Sep. 1996.

[13] J. Levin, N. O. Pérez-Arancibia, P. A. Ioannou, and T.-C. Tsao, "A Neural-Networks-Based Adaptive Disturbance Rejection Method and Its Application to the Control of Hard Disk Drives," *IEEE Trans. Magn.*, vol. 45, no. 5, pp. 2140–2150, May 2009.

[14] P. S. Sreetharan and R. J. Wood, "Passive Aerodynamic Drag Balancing in a Flapping-Wing Robotic Insect," *J. Mech. Design*, vol. 132, no. 5, pp. 051 006–1–11, May 2010.

[15] R. J. Wood, K.-J. Cho, and K. Hoffman, "A novel multi-axis force sensor for microrobotics applications," *Smart Mater. Struct.*, vol. 18, no. 12, pp. 125 002–1–7, Dec. 2009.

[16] Y. M. Ho, G. Xu, and T. Kailath, "Fast Identification of State-Space Models via Exploitation of Displacement Structure," *IEEE Trans. Autom. Control*, vol. 39, no. 10, pp. 2004–2017, Oct. 1994.

[17] N. O. Pérez Arancibia, S. Gibson, and T.-C. Tsao, "Adaptive Control of MEMS Mirrors for Beam Steering," in *Proc. ASME Int. Mech. Eng. Cong. Expo.*, Anaheim, CA, Nov. 2004, IMECE2004–60256.

[18] N. O. Pérez Arancibia, *Adaptive Control of Opto-Electro-Mechanical Systems for Broadband Disturbance Rejection*. Los Angeles, CA: Ph.D. Dissertation, University of California, Los Angeles, 2007.

[19] G. E. Dullerud and F. Paganini, *A Course in Robust Control Theory*. New York, NY: Springer-Verlag, 2000.

[20] A. J. Laub, M. T. Heath, C. C. Paige, and R. C. Ward, "Computation of System Balancing Transformations and Other Applications of Simultaneous Diagonalization Algorithms," *IEEE Trans. Autom. Control*, vol. 32, no. 2, pp. 115–122, Feb. 1987.

[21] D. Chen and B. Paden, "Adaptive Linearization of Hybrid Step Motors: Stability Analysis," *IEEE Trans. Autom. Control*, vol. 38, no. 6, pp. 874–887, Jun. 1993.